Chapter 5
Nanomaterials Behavior in Corrosion Environments

Abstract The main aspects of the materials corrosion are considered taking special attention to some specific material behavior associated with the nanostructure. The NMs properties and behavior in the various corrosion media are generalized including the combined actions and high-temperature oxidation. Attention is paid to the role of size factor in reactions of nanostructures with an environment as well as to the theoretical approaches and modeling by MD methods. Some examples of the NMs exploitation in the corrosive media are given and several poorly understood phenomena are mentioned.

5.1 General Considerations

In practice, almost any use of materials relates to the interaction with some environment and it always requires accounting and prevention of corrosion. The corrosive interactions problem is of particular importance for NMs due to their non-equilibrium state. From a general view point, the presence of large number of interfaces (such as GBs and TJs), on one hand, must affect on the materials corrosion performance, because these sites (with their disordered structure) are subjected to the selective interactions with an aggressive media. On the other hand, the diffusion-controlled formation of the protective surface films (i.e., surface passivation) at these interfaces can proceed more intensively that can prevent the further spread of corrosion. General effect of some material interaction with an environment is determined by relation of these two factors and depends on reaction parameters (their kinetic rate constants), as well as on the nanostructure parameters. In this situation, the NMs can be both more or lesser corrosion-resistant in comparison with their CG counterparts, and the non-trivial situation has led to many conflicting results, related to the NMs corrosive and electrochemical behavior, that was especially noted in monograph [1] and some recent reviews (e.g., [2–7]).

R.A. Andrievski and A.V. Khatchoyan, *Nanomaterials in Extreme Environments*,
Springer Series in Materials Science 230, DOI 10.1007/978-3-319-25331-2_5

It seems useful to remind how the volume fractions of the GBs, TJs, and total interface area depend on the crystallite sizes. These dependences shown in Fig. 5.1 (adapted from [8]) have been derived in a frame of some model, where the grains were approximated by tetrahedral dodecahedrons divided by the intergrain boundaries of 1 nm thick.

The curves in Fig. 5.1 show that the contribution of interfaces becomes substantial when the GS is below 60–70 nm, but the TJs fraction is prevailing for the GS less than 3 nm. The total fraction of interfaces achieves 50 % for GS about 6 nm.

For example, consider the opposite influence of the GS on the oxidation resistance and compare the behavior of Fe–Cr alloy and nickel under oxidation. The curves presented in Fig. 5.2 illustrate that the transition to nanostructure is

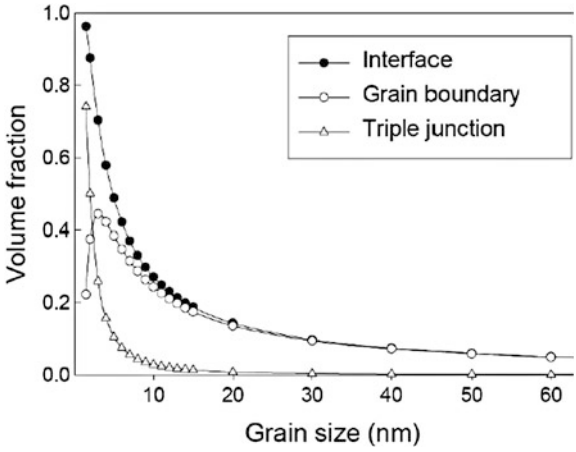

Fig. 5.1 Volume fractions of total interfaces, GBs, and TJs as a function of GS

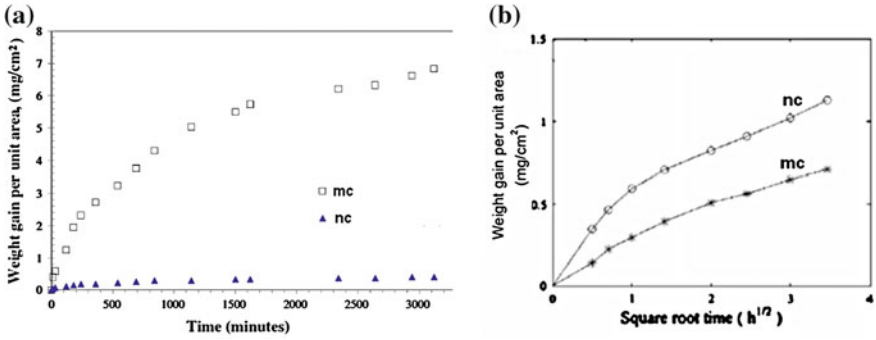

Fig. 5.2 Oxidation kinetics of nanocrystalline (*nc*) and microcrystalline (*mc*) specimens of Fe–10 wt% Cr (T = 400 °C) (**a**) and Ni (T = 700 °C) (**b**)

accompanied with the oxidation rate decrease for alloy, but the opposite tendency has been revealed for pure nickel (adapted from [9, 10]).

The emphasis of the studies [9, 10] was on the sample attestation and preparation by sintering of the Fe–Cr nanopowders and electrodeposition of Ni. The GS in the studied samples were of 52 ± 4 nm (nanocrystals) and about 1.5 μm (microcrystal) for Fe–Cr alloy, as well as of ∼28 nm (nanocrystals) and about 3.4 μm (microcrystals) for Ni. A comparison with data of Fig. 5.1 is demonstrating that the GS of the samples used in [9, 10] were quite representative ones. The secondary ion spectroscopy measurements have shown that the chromium and oxygen content in the surface layers of the oxidized nanostructured Fe–Cr alloys is higher than that in the microcrystalline objects. This fact confirmed a conclusion that, in these systems, a passivating oxide film formation (preventing the nanocrystalline samples corrosion) proceeds more intensively as exemplified by the kinetic curves of Fig. 5.2a. The analogous estimations of a prevailing total diffusion flux (including the Cr partial coefficients of volume/boundary diffusion) were presented in review [11]. It is important that the lowest values of oxidation rates for the Fe–Cr nanoalloys are retained in the samples with a bimodal structure (nc + mc = 50/50) usually characterized by the high strength and plasticity [12]. For the nanocrystalline nickel samples, it was demonstrated that the accelerated NiO film formation is also explainable with Ni boundary diffusion, but this film is not passivating one.

The above given examples readily illustrate an important role of the GS factor on the NMs oxidation process, but for general consideration, it is necessary to keep in mind a very complicated character of the corrosion effects in a whole, because they include, for example, the pitting (i.e., formations of the pointed or localized corrosion sites), corrosion stress cracking, electrochemical interactions, the evolutional changes of the passivating films, galvanic pairs formation, and many other complex processes. The bibliography of studies in this field is very extensive, and therefore, considering the NMs behavior under extremes, only the most reliable and certain experimental results, obtained for the well attested samples, will be referred to. The more detailed information can be found in reviews [2–7].

In liquid media, the corrosion is studied mainly by the electrochemical methods using so- called anode and cathode characteristics curves of the $E = \mathrm{f}\,(\lg i_a)$ type, where E is a potential and i_a is a velocity of anodic reaction, expressed by units of current density. From these characteristics, the main corrosion process parameters (such as the corrosion and passivation potentials, corresponding currents, etc.) can be determined and analyzed. The linear part of so- called the Tafel's curves is always used for the corrosion process rates determination and has a simple form:

$$E = a + b \lg i_a, \tag{5.1}$$

where a and b are some constants.

5.2 Main Experimental Results

5.2.1 Metals and Alloys

5.2.1.1 Nickel, Cobalt and Cupper

Some episodic studies of the NMs corrosion properties and special characteristics began more than 30 years ago. The first systematic study has been devoted to the electrochemical behavior of the nanocrystalline nickel samples of very high purity (99.99 %) in 2N H_2SO_4 at 293 K [13], but it is of interest that the results were published only in 1991 year. The study itself has been devoted to a comprehensive investigation of the electrodeposited nickel tapes having the high physical and mechanical characteristics [8]. In Fig. 5.3, the anodic polarization curves for nano/CG samples are presented and some passivation characteristics derived from these curves are given in Table 5.1 (adapted from [13]).

The data demonstrate that the transition to nanostructure is accompanied by an increase the corrosion and passivation potentials (E_{corr} and E_p) characteristic values. The rising of two other important parameters (namely, the critical passivation current i_a and passive state current i_p densities) shows that the electrochemical

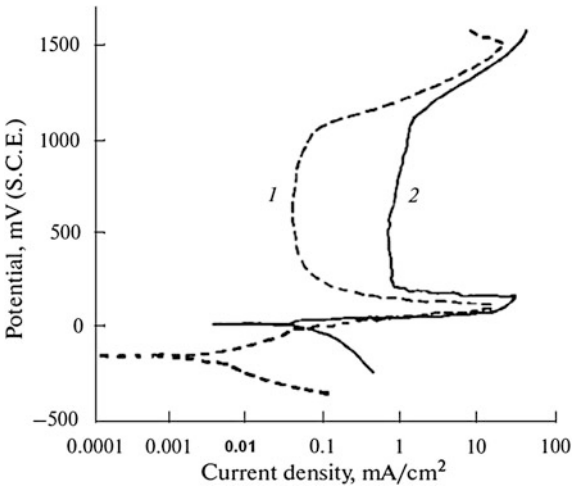

Fig. 5.3 Potentiodynamic anodic polarization curves for Ni in poly- and nanocrystalline state (*1* GS of 100 μm; *2* GS of 32 nm) in 2N H_2SO_4 at 293 K. A saturated calomel electrode was used as a reference electrode

Table 5.1 Passivation characteristics of nickel specimens with different GS (L) according to the data of polarization measurements in 2N H_2SO_4

L (nm)	Corrosion potential E_{corr} (mV)	Passivation potential E_p (mV)	Peak active current density i_a (μA/cm^2)	Minimum passive current density i_p (μA/cm^2)
10^6	−170.0	+113	13,370	32.7
32	+7	+158	26,120	580

resistance of nanocrystalline nickel in 2N H_2SO_4 is lower in comparison with the CG nickel as similar to its oxidation resistance (see Fig. 5.2b). The SEM studies have shown that the GBs and TJs are markedly dissolved under such conditions but the corrosion localizations were higher for the CG samples. It was found also that nanostructurization of the nickel samples is catalyzing the hydrogen impurities release as well as retarding the passivation kinetics and decreasing a stability of the formed passivating films. The range of the studied GS was later widened [14] to the smaller values (L = 28, 22, 10 and 8 nm) and the results obtained have largely confirmed the main results of [13], namely, a growth of E_p and i_p values with the GS decreasing. It was marked in review [8] that the commercial fabrication of the studied nanocrystalline nickel bands (in spite of some decrease of their corrosive resistance) was organized in Canada and they had a widespread use for coating and cladding for the various items in power-engineering and other technical fields.

The comparison of the corrosion effects in the nano/CG cobalt samples ($L \sim$ 12 nm and $L \sim$ 8 μm, respectively) in 0.25M Na_2SO_4 solution (pH of 6.5) has shown that the GS decrease is only slightly influencing on the material corrosion resistance [15]. However, for the copper electrochemical corrosion in 0.1M HNO_3, a transition to the nanostructure (namely from GS of ~300 μm to L about 20 nm) is accompanied by more active dissolution without any passivation, that can be explained by a presence of numerous GBs, TJs, microvoids, and weak links at certain interfaces between grains [16]. In addition, for the general analyze of the GS influence on the material corrosion resistance, the considerations must be given to many other factors, such as the residual stresses, the impurity localization (for example, sulfur) on the grain boundaries, the surface roughness and texture, the pores presence, the passivating layers stability, etc. These numerous and various material features often lead to the non-monotonic characteristics of the corrosion resistance under a grain refinement or to a reduction of the real size effects [3, 7, 17].

In connection with a diversity of these influencing factors, it is of interest to consider the results of the Cu foils behavior (with both the nanotwinned and microcrystalline structure) in 3.5 % NaCl solution (pH ~ 8.0), presented in Table 5.2 (adapted from [18]).

Table 5.2 Summary of corrosion test of nanotwinned and microcrystalline Cu foils with common thickness of ~25 μm

Type	Grain size (μm)	% grains with with na- notwins	Area fraction of grain {111} orientation	Polarization resistance (kΩ cm^2)	Corrosion cur-rent density (μA cm^{-2})	Passivation current density (mA cm^{-2})
I	0.52	90	0.88	28.6 ± 7.1	0.34 ± 0.09	1.15 ± 0.20
II	0.41	60	0.33	10.2 ± 4.4	1.08 ± 0.39	1.14 ± 0.23
III	0.34	5	0.08	10.4 ± 0.5	1.26 ± 0.06	1.08 ± 0.27
IV	8.6	0	0.02	9.2 ± 2.1	1.92 ± 0.42	1.27 ± 0.18

The data readily manifest that namely the films with high concentration of the nanotwinned grains and their area fraction with the {111}-texture demonstrated the highest corrosion resistance though the passivation current densities values were the same for all objects. The investigations of the protective passivating layers content (including both the electrochemical corrosion studies and immersion experiments) detected a presence of the Cu_2O columnar (bar) crystals with the {111}-texture, but a minimal pitting was observed in the type I foils. It is interesting that the corrosion characteristics of III and IV type foils (in spite of the GS difference about one order of magnitude) are very similar, i.e., in the experiments [18] the GS factor was not an important one.

5.2.1.2 Iron and Steels

These objects are well studied (e.g., papers [9, 12, 19–23], reviews [1–7, 11] and references therein), and therefore we will give attention to the last results in brief. A wide investigation of electrochemical properties of the α-Fe + Fe_3C nanocrystalline composites in some sulfuric and hydrochloric acid media was carried out by authors [19] for samples prepared by mechanosynthesis from the carbonyl Fe and carbon mixtures followed by a dynamic pressing. In the Table 5.3 (adapted from [19]), the detailed data are presented concerning the characterization and properties of numerous composites including the compact samples of pure Fe and steel with carbon content of 1.3 mass%.

The analysis of the obtained polarization curves and values of E_{corr} and i_a has shown that for the $Fe_{95}C_5$ and Fe–1.3 % C samples the transition to nanocrystalline state is markedly influencing the active dissolution process (that can be obviously explained by the GBs number growth), but from other side, annealing of the $Fe_{95}C_5$

Table 5.3 Characterization and electrochemical properties of (α-Fe + Fe_3C) composites in 0.05M H_2SO_4 + 0.45M Na2SO4

Composite	Phase content (wt%)		Grain size (nm)		Parameters of polarization curves			
	α-Fe	Fe_3C	α-Fe	Fe_3C	E_{corr} (mV)	i_c(−400 mV) (mA/cm^2)	i_a (−200 mV) (mA/cm^2)	i_p (1250 mV) (mA/cm^2)
Pure Fe	100	–	$300 \cdot 10^4$	–	−325	0.6	35.20	0.05
Fe–1.3 %C	~91	~9	$2 \cdot 10^4$	n/d	−305	1.6	45.2	0.1
$Fe_{95}C_5$	91	9	38	48	−385	1.1	65.4	1.4
Annealing at 800 °C	91	9	n/d	n/d	−305	5.7	48.1	1.8
$Fe_{90}C_{10}$	84	16	40	49	−385	1.8	99.7	4.5
$Fe_{85}C_{15}$	45	55	49	47	−325	7.8	26.2	1.0
$Fe_{75}C_{25}$	8	92	42	29	−195	26.2	~0	3.9

E_{corr} is a corrosion potential; i_c, i_a and i_p are cathodic, anodic and passivation current densities at different potentials, respectively

samples, leading to the GS growth, is leveling the difference with the Fe–1.3 % C steel regarding the values of E_{corr} and i_a. The microscopic studies have shown also an important role of a forming cementite morphology, because the protective role of the γ-FeOOH and Fe_2O_3 passivating films is decreasing due to carbon accumulation at the interfaces resulting from the cementite decomposition. The authors [18] concluded that namely the cementite (Fe_3C) content makes the greatest impact on the electrochemical behavior of the studied composites and this influence exhibits itself not only in the anode and cathode current values, but also in the growth of the pitting resistance and a catalytic activity in the hydrogen release reaction.

In some works, a positive effect of nanocrystallinity on corrosion resistance of the pure iron and its chromium alloys has been demonstrated. For example, in [22] there has been shown, that the electrochemical resistance of the nanocrystal Fe samples (L = 50–89 nm) in the (0.1–0.4)M HCl solutions is increasing as compared with the CG counterparts ($L \sim 50$ μm). The similar results (with the GS decrease from 750 to 32 nm) were obtained for the Fe electrochemical corrosion in near-neutral aqueous solution containing corrosion inhibitor like sodium benzoate [20]. A transition to the nanostructures for the Fe–(10, 20)% Cr alloys was accompanied with more active passivation and formation of a protective Cr_2O_3 film, leading to improvement of the electrochemical corrosion resistance in 0.5M H_2SO_4 [23], that qualitatively corresponds to the above given results (Fig. 5.2a) for these alloys oxidation [9].

5.2.1.3 Titanium and Zirconium

In a CG state, these two metals under aggressive environment are coated by some oxide protective films impeding any corrosion development. Therefore, these metals transition to a nanocrystalline state is accompanied with various phenomena, connected with passivation processes, which were a subject of many investigations (e.g., [24–31]). The comparison of the electrochemical behavior for both nanostructured and CG samples demonstrates an important role of the Ti texture (arising at different modes of ECAP and HPT actions) and a non-monotonic influence of the GS. Such non-monotonic kinetic changes for the corrosion resistance of microscopic samples were observed also for Ti and Ti–V–Al alloys, as well as corrosion resistance rise for alloys after ECAP [26, 27]. The detailed studies of the electrochemical properties and corrosion resistance of the CG ($L \sim 15$ μm) and submicrocrystalline ($L \sim 0.15$ and 0.46 μm) samples in the (1–5)M H_2SO_4 have demonstrated some important differences in the anode and cathode process rates and other parameters [28]. In Fig. 5.4, the kinetic curves of the mass change per unite surface area are presented for different titanium samples in 5M H_2SO_4 at 23 °C (adapted from [28]).

As it can be seen from the Fig. 5.4, an induction period is a characteristic for the microcrystalline samples only, but in one of them (the sample with smallest GS, curve 3) the corrosion instead of decay becomes very intense and dominates in the

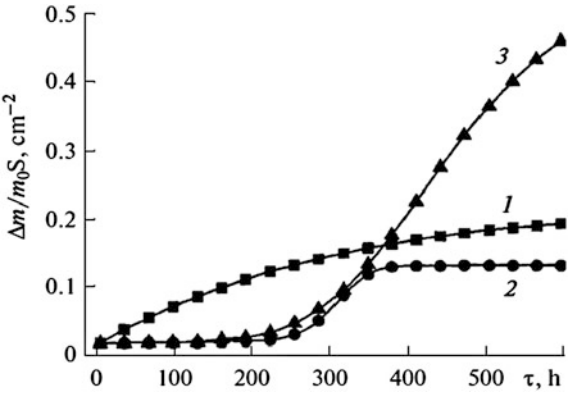

Fig. 5.4 Time dependence of the relative change in weight upon corrosion in 5M H_2SO_4 of Ti specimens with different GS: (*1*) L = 15 μm; (*2*) L = 0.46 μm; (*3*) L = 0.15 μm

Table 5.4 Corrosion current density (i_{corr}) and corrosion rate (on the weight loss results after 720 h duration) of different $Ti_{60}Ni_{40}$ specimens in 1M NaCl

Specimen	Grain size (nm)	i_{corr} (mA/cm^2)	Corrosion rate (mm/year)
Nanocrystalline multi-phase (Ti_2Ni + Ti + TiNi)	35 ± 5	$1.5 \cdot 10^{-3}$	0.066
Amorphous ($Ti_{60}Ni_{40}$)	–	$8.3 \cdot 10^{-4}$	0.029
Nanocrystalline (Ti_2Ni)	10 ± 5	$4.0 \cdot 10^{-4}$	0.017

GS sample. The mechanism of this phenomenon is interesting and needs new research efforts.

The thermographic studies of oxidation these objects have shown that in the polythermal mode up to $T \sim 1000$ °C, the weight changes are practically the same for all samples, and only at higher temperatures the microcrystalline samples are oxidizing more intensively [29]. It was found also that the microstructure, formed in Ti under deformation effects, promotes more active oxygen dissolution and stabilization of α-phase by shifting the α → β polymorphic transition point to the high temperature range.

The electrochemical behavior and immersion corrosion of the nanocrystalline and amorphous intermetallic $Ti_{60}Ni_{40}$ samples in 1M NaCl aqueous medium (T = 20 °C) were studied and compared in [30]. The data are presented in Table 5.4 (adapted from [30]).

The results show that the substantially more positive results in the both corrosion tests were obtained for the single phase nanocrystalline samples. The XPS studies have demonstrated that only in this case the TiO_2 film is formed over the sample surface (in other samples their surfaces contained the TiO and Ti_2O_3 oxide admixtures as well as metallic titanium).

In [31], the ECAP (4 passes at T = 460 °C) influence was detected for one of the most important material characteristics (namely, stress corrosion cracking) by the example of Zr–2.5 wt% Nb alloy widely used in the nuclear technique. As the

Table 5.5 Structure parameters and the strength/elongation change of Zr–2.5 wt% Nb alloy after the stress corrosion cracking tests

Specimen treatment	Structure parameters: L is a GS, N_{pitt} is a number of pittings, and d_{pitt} is a pitting diameter			Temporal fracture resistance (σ_t) and elongation (δ) before (numerator) and after (denominator) tests			
	L (nm)	N_{pitt}	d_{pitt} (nm)	σ_t (MPa)	$\Delta\sigma_t/\sigma_t$ (%)	δ (%)	$\Delta\delta/\delta$ (%)
ECAP	200–700	115 ± 12	5 ± 2	700/665	5	10/9	10
Annealing (1)	400–1100	60 ± 6	16 ± 2	680/545	20	15/9	40
Annealing (2)	500–1500	9 ± 5	14 ± 2	620/510	18	25/17	32

corrosive medium, 1 % iodine solution in methanol was used, the stress level corresponds to 0.8 of the yield strength limit, the temperature equals to 20 ± 2 °C and the test duration was 50 h. For comparison, the samples annealed by two modes were used: (1) 530 °C (1 h) and (2) 530 °C (1 h) + 560 °C (3 h). The sample characterization and test results are presented in Table 5.5 (adapted from [31]).

From these data, we notice that the losses in mechanical properties are significantly lower for the samples treated by ECAP. However, the results are not solid, because of numerous nanosized pitting defects were detected in these samples, which under durable tests can be converted into the microscopic cracks or fracture sites, that maybe will cardinally change the whole situation of the described mechanical properties degradation after the samples testing.

5.2.1.4 Aluminum, Magnesium and Zink

It is interesting to note that earlier the specialists (for example, authors of review [2]), when considered some inconsistency of the results concerning the GS influence on a material corrosion behavior (in Al, Mg and their alloys), paid their main attention to the systems with micrometric GS, but lately the interest has been clearly shifted to the so-called ultrafine-grained (UFG) materials. Nevertheless, the nanostructurization of low-melting metals by SPD methods as before remains connected with a complex and hard problem, because of the intensive dynamic recrystallization. The electrochemical tests of Al–4 wt% Mg–0.8 % Si alloy samples in sea water have discovered that the GS refinement from of 7 μm to about 0.4 μm leads to the polarization resistance growth about 1.5 times [32], but at the same time, the stress corrosion cracking turned to be substantially below for the CG samples. After 4 passes of ECAP, the GS of AA2024-T351(Al–4.15 % Cu–1.14 % Mg) alloy decreases approximately to 200 μm and it manifests itself during transition from an intercrystalline corrosion mode to a pitting one under tests in 0.5 M NaCl solution [33]. In samples of the magnesium AZ31 alloy (Mg–3.62 % Al–1.36 % Zn), the GS achieved about 1 μm after 8 passes of ECAP. The ECAP treated samples were characterized by a greater uniformity and homogeneity, and their corrosion

resistance in 0.1 M NaCl solution (exposure time is of 168 h) was higher as compared with the initial CG samples [34].

The increase of the electrochemical corrosion resistance with the GS diminishing in the range from of 5–20 μm to about 40–60 nm was detected also for the electrodeposited micro- and nanostructured zinc coatings [35, 36].

5.2.2 *High-Melting Point Compounds*

Conventionally, a HMPC group includes carbides, borides, nitrides, oxides and other substances with the melting point temperature T_M above 2000 °C. The thermal, radiation and deformation stability of such nanocrystalline objects was considered in early Chaps. 2–4. Below, we analyze a behavior of such materials in some liquid media and under a high-temperature oxidation.

5.2.2.1 Behavior in Liquid Media

In general, the problem of HMPC corrosion (including the high-temperature oxidation processes) was studied by Lavrenko and his coworkers (e.g., [37–41]). As an example, in Fig. 5.5, the anode polarization curves are presented for the amorphous and amorphous-nanocrystalline TiB_2 films as well as CG hot-pressed samples tested in sea water at room temperature.

It was supposed [40] that the TiB_2 anode oxidation can be described by the following system of reactions:

$$TiB_2 + 7H_2O \rightarrow TiO^{2+} + 2BO_3{}^{3-} + 14H^+ + 10e, \tag{5.2}$$

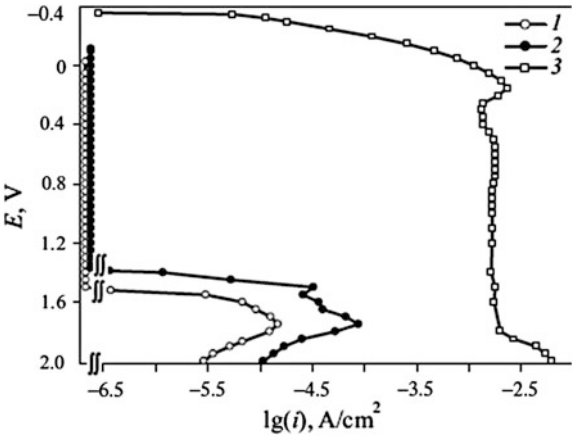

Fig. 5.5 Anodic polarization curves of TiB_2 amorphous (*1*), amorphous-nanocrystalline (*2*) and CG (*3*) specimens (adapted from [40])

$$TiB_2 + 6H_2O \rightarrow Ti^{3+} + 2BO_3{}^{3-} + 12H^+ + 9e, \quad (5.3)$$

$$TiB_2 + 8H_2O \rightarrow TiO_2 + 2BO_3{}^{3-} + 16H^+ + 10e, \quad (5.4)$$

where the first reaction (5.2) corresponds to the more sloping parts of the polarization curves (1 and 2) and reflects a partial electrochemical dissolution of titanium diboride. The steeper part of these curves corresponds to the trivalent titanium ions transitions into solution by the reaction (5.3) and the final passivation process is connected with the TiO_2 (rutile modification) formation by the reaction (5.4). The results of analysis for the properties (before and after the electrochemical testing) allow to give several common conclusions:

1. Corrosion resistance of the TiB_2 CG samples is sufficiently low as compared with their film counterparts.
2. Corrosion resistance of amorphous films is one order of magnitude higher than that for the amorphous-crystalline films containing various boride phases (such as TiB_2, TiB and other compounds) with GS in the 15–90 nm range.
3. In the studied film thickness range (70–250 nm), the corrosion resistance and passivation potential of the amorphous films increase with their thickness.
4. The films oxidation proceeds by the pitting corrosion mechanisms and the TiO_2 formation is fixed inside the pittings. Such pitting-type character of corrosion for the amorphous-crystalline TiB_2 films and their high corrosion resistance were described also in [42].

The similar and analogous results were obtained also in studies of the TiN films electrochemical corrosion [41], and an essential growth of the corrosion resistance was fixed in many other investigations of the nitride films behavior in liquid media of sea water type. Some recent results of these studies are presented in the following studies, devoted to the titanium nitride and alloys in its base [43–46], as well as to the zirconium, hafnium, vanadium, and chromium nitrides [47–50]. The data of Table 5.6 illustrates the various characteristics of the TiN films being deposited at different temperatures on stainless 304 steel surface by a magnetron sputtering method. These results pronouncedly demonstrate that the film thickness decrease leads to substantial growth of their corrosion resistance in 0.5M H_2SO_4 solution, and this effect can be connected with a so- called fine-grained morphology under

Table 5.6 Effect of different substrate temperature (T_S) on the TiN films thickness (δ), surface roughness (*RMS* is root-mean-square value) and corrosion characteristics (E_{corr}, i_{corr} and corrosion rate) (adapted from [44])

T_S (°C)	δ (nm)	RMS (nm)	E_{corr} (V)	i_{corr} (μA/cm^2)	Corrosion rate (mm/year)
25	205	3.95	0.433	9.1	0.0947
100	181	1.84	0.489	7.48	0.0775
200	152	1.71	0.469	3.73	0.0390
300	137	1.62	0.523	1.78	0.0181

the deposition temperature rise. It is characteristic that the corrosion resistance growth is accompanied with some increase of the materials wear resistance (e.g., [45–47, 49]).

5.2.2.2 High-Temperature Oxidation

Some results, concerning the oxidation of the HMPC films, were presented above as applied to the cutting materials in Chaps. 2 and 4 (see Figs. 2.7–2.9 and 4.14). An interest to these investigations is now rising in connection with the special materials for hypersonic aviation (the fairings, wing leading sharp edges, propulsion system components, etc.). The oxidation, degradation and corrosion behavior of many composite materials-based ZrB_2, HfB_2, SiC, $MoSi_2$, and other compounds are now investigated at the very wide temperature range (e.g., [51–53]). These materials are now called as the ultra-high temperature ceramics. It must be noted that a role of size effects (both at the micro- and nano levels) in bulk samples of these materials practically remains unexplored, and therefore below, we give some examples of the nanoparticles and films behavior at oxidation.

In Fig. 5.6 (adapted from [54]), three different exothermic peaks are very pronounced for the TiC micro- and nanoparticles (in details, they are described below in Table 5.7).

The data show that the particles of similar stoichiometry have only few differences in chemical composition and their particle sizes (evaluated by BET methods) are differ in 800 times. Nevertheless, the phase formation during oxidation (fixed by

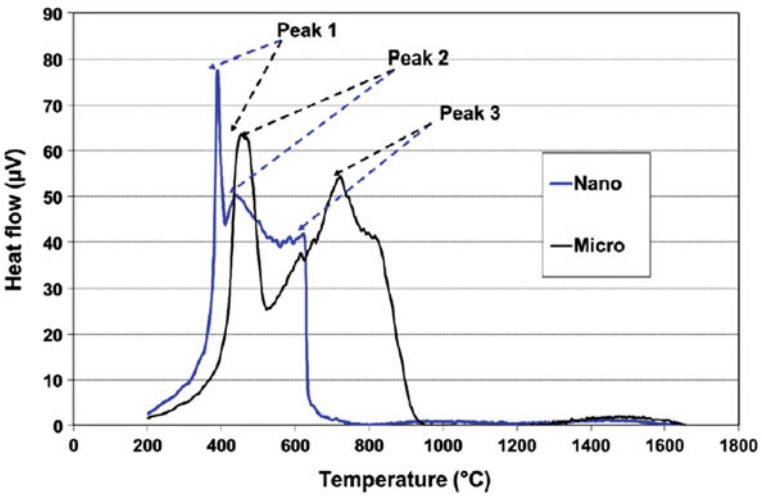

Fig. 5.6 The evolution of heat flow as a function of DTA temperature for TiC nano- and microparticles (see Table 5.7)

Table 5.7 Characterization of TiC particles and temperature range of phase occurrence during oxidation (adapted from [54])

Particle type	Formula	Diameter (nm)	Temperature range (°C) of phase occurrence during oxidation				
			TiC	TiC_xO_{1-x}	Ti_3O_5	TiO_2 (anatase)	TiO_2 (rutile)
Nano	$TiC_{0.9}O_{0,23}N_{0.10}$	53	<300	<390	330; 620	620; 800	>800
Micro	$TiC_{1.0}O_{0.04}N_{0.01}$	$4 \cdot 10^3$	<300	<460	400; 720	720; 900	>900

XRD) was a similar type with characteristic shift to the lower temperatures just for nanoparticles.

The study of the WC micro- and nanoparticles oxidation in a wide range of sizes (from about 20 to of 2000 nm) and temperature interval (323–1173 K) has shown that the WC → W_2O_3 transition (without WO_2 formation) does not depend on the particles dispersity character [55]. The oxidation rate was proportional to $1/\langle d \rangle$, where $\langle d \rangle$ is the average particle size, and the oxidation process activation energy was falling from value of ∼120 kJ/mol to about 90 kJ/mol with the particle size diminishing from about 2000 nm to approximately 20 nm.

The diboride oxidation is describing by several reactions from which, especially for TiB_2, we can single out the following ones:

$$3TiB_2 + 7O_2 \rightarrow TiO_2 + 2B_2O_3 + 2TiBO_3, \tag{5.5}$$

$$4TiB_2 + 9O_2 \rightarrow 4TiBO_3 + 2B_2O_3, \tag{5.6}$$

$$4TiBO_3 + O_2 \rightarrow 4TiO_2 + 2B_2O_3, \tag{5.7}$$

$$2TiB_2 + 5O_2 \rightarrow 2TiO_2 + 2B_2O_3. \tag{5.8}$$

The boron oxide and titanium borate formation usually is fixed by the XRD, DTA/TGA methods, and so on. The characteristic feature of the (5.5–5.8) reactions is the evaporation of the low-melting boron oxide, imposing a specific influence on the TiO_2 passivating films formation. The admixture role in a shift of the TiO_2 film high-temperature formation was marked also in [37] for the different in composition TiB_2 powders. The powders and compacts with a higher content of metallic admixtures (such as Fe, Ni, Mo and others) turned to be more stable to oxidation in the 700–1200 °C range and, for them, the high-temperature peak at the DTA/TGA thermograms was fixed at about 80 °C higher in comparison with their more pure counterparts. This fact can be naturally connected with the interface enrichment by the metallic admixtures followed by formation of a diffusion barrier inhibiting further oxidation process. The TEM observations in situ of the ZrB_2 nanoparticles (with size of ∼35 nm) oxidation behavior at temperature of 1500 °C have revealed the reaction of (5.8)-type with formation of a ZrO_2 tetragonal modification and evaporation of B_2O_3 [56].

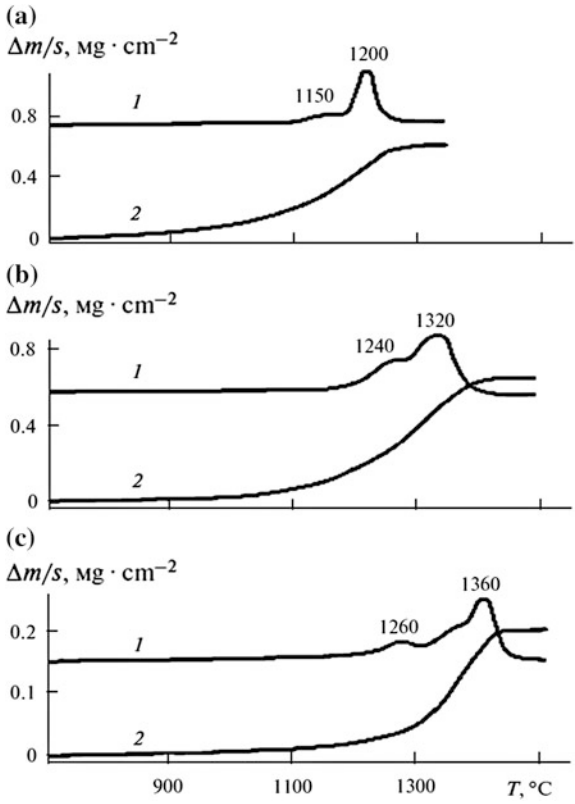

Fig. 5.7 DTA (*1*) and TGA (*2*) curves of the oxidation of films I (**a**), II (**b**) and III (**c**)

Let us consider some results of the film oxidation studies supplementary to above presented data of Chaps. 2 and 4. In Fig. 5.7, the DTA/TGA curves are presented for oxidation of the multicomponent films, obtained by a magnetron sputtering using the targets with different composition (in wt%): AlN + 50TiN (film **I**), AlN + 50TiB_2 (film **II**) and AlN + 10TiB_2 + 20SiC (film **III**) (adapted from [38]).

These data show that, under the study heating conditions (15 °C/min), a marked oxidation process for the films **I**, **II** and **III** is fixed at the temperature of ~750, ~950 and ~1020 °C, respectively. It is obvious also that film **III** demonstrates the highest oxidation resistance. These data comparison with the results for CG samples, being oxidized under the same conditions, shows that the values of specific mass gain under oxidation for the film samples are lower in 4–5 times.

Below, in general form, is written down the main reactions proceeding under the **I–III** type films oxidation:

film **I**

$$2(Ti_{1-y}Al_y)N_x + (2 - y/2)O_2 \rightarrow 2(1 - y/2)TiO_2 + yAl_2O_3 + xN_2, \quad (5.9)$$

$$TiO_2 + Al_2O_3 \rightarrow Al_2TiO_5; \quad (5.10)$$

film **II**

$$2TiB_2 + 5O_2 \rightarrow 2TiO_2 + 2B_2O_3, \quad (5.11)$$

$$4AlN + 3O_2 \rightarrow 2Al_2O_3 + 2N_2, \quad (5.12)$$

$$2Al_2O_3 + B_2O_3 \rightarrow Al_4B_2O_9, \quad (5.13)$$

$$9Al_2O_3 + 2B_2O_3 \rightarrow Al_{18}B_4O_{33} \quad (5.14)$$

and reaction (5.10);

film **III**

$$SiC + 2O_2 \rightarrow SiO_2 + CO_2, \quad (5.15)$$

$$3Al_2O_3 + 2SiO_2 \rightarrow 3Al_2O_32SiO_2 \quad (5.16)$$

and reactions (5.10–5.14).

In these reaction sets, no account has been taken to a possible admixture influence, such as iron (always connected with the powder samples grinding under target production), the non-stoichiometric phase formation, nitrogen reactions, etc. From the general considerations, it is obvious that the studied process of high-temperature films interaction with air is a multi-stage one. An oxidation initial stage practically for all films begins with a formation of the rutile and boron oxide layers (for films **II** and **III**). With allowance made for the known data, regarding to the oxidation processes in the CG objects with the same composition, the DTA curve peak at 1200 °C for film **I** can be associated with the reaction (5.10), but the peaks at 1240 and 1320 °C (film **II**) most probably correspond to the (5.13, 5.14 and 5.10) reactions. The peaks at 1260 and 1390 °C (for film **III**) relate to the reactions (5.15 and 5.12), connected with the β-crystobalite and α-alumina formation, while the peak at 1390 °C corresponds to the reactions (5.10 and 5.16) with formation of aluminum titanate and mullite (the last two reactions most likely define a protective layer composition for the film **III**). The material phase compositions obtained in the reactions (5.13) and (5.14), however, are partly verified only by the XRD data, maybe because the films are very thin and the total phase amount remains low for correct registration.

The results of microspectral X-ray analysis, obtained by scanning the 0.2 mm-length film surface sections, are confirmed in the films **I–III** after oxidation a presence of some phase near by content to aluminum titanate. An EDA detected also confirmed that the surface layers are enriched by aluminum and depleted by titanium. The fracture surface analysis of the films has shown a formation of some nanocolumnars with the characteristic sizes of ~100 nm. Moreover, this phenomena was observed only in the films **III** whereas such nanocolumnars were absent in films **I** and **II**, and for them, the structure inclusion dimensions after oxidation were in the range 300–600 nm.

Hence, the high scaling resistance, detected for the film **III,** can be explained by enrichment of the surface with aluminum and a stable protective layer formation. In this case, the nanocolumnar formation is assisting to nanocrystalline structure conservation and more intensive diffusion mobility. It maybe supposed that namely nanostructures, as in given above results (Fig. 5.2a) [9], are ensuring a more intensive formation of the stable protective layer.

The oxidation processes and corrosion resistance comparison for the simple and complex HMPC films was carried out and analyzed in [57]. Figure 5.8 shows some advantages of the amorphous films over the crystalline ones.

Though the Fig. 5.8 results relate only to the short-time experiment durations, but in general, they seem to be correct. It is interesting that the Si–B–C–N based films on the sapphire and silicon carbide substrates remained stable up to temperatures of 1700 °C.

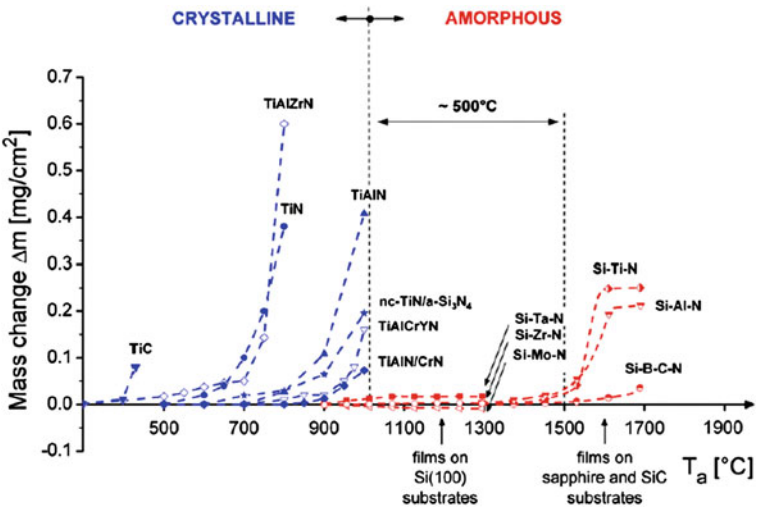

Fig. 5.8 Oxidation resistance of crystalline and amorphous films-based HMPC (adapted from [57])

5.3 Some Theoretical Approaches and Modeling

The results of many cited studies (e.g., [9, 12, 18, 23, 27, 39–41, 45–47, 57]) are clearly demonstrating that various studied NMs really have the high corrosion and oxidation resistance characteristics. However, these results do not give a comprehensive idea of the GBs, TJs, grain inner areas or other peculiarities role in the investigated systems, and while these studies remain predominantly at the empirical level. The theoretical investigations are very few.

Some results, obtained for nanocrystalline zirconium oxidation kinetics in the 200–500 °C range and calculated with taking into account the electronic mean free pass, are presented partly in Fig. 5.9 [58]. They show a data good agreement for the CG samples and a general decrease of the zirconium oxidation rate with the decrease of GS.

A relationship between the GS and corrosion rate of metals, similar to the known formulae of Hall-Petch (see early (4.4)), was proposed in [59] and has a form:

$$i_{\text{corr}} = (A) + (B)L^{-1/2}, \tag{5.17}$$

where i_{corr} is the corrosion current density (the value proportional to corrosion rate), A is the constant which is likely proportional of the environment and B represents a material constant according composition and impurity level. This relationship is based on the experimental data extension and generalization for the CG Mg and Al alloys, but its physical foundations remain still elusive.

The approximations in the DFT method frame have shown that the TiB_2 nanocrystals are stable with respect to water molecules and thus can be reckoned as resistant to attack by the various biological media [60]. The examples of the DFT usage for to describe the passivity films breakdown are presented in review [5] as an example for a Cl interaction with hydroxylated NiO [61]. The theoretical consideration and comparison of the one- and multi-layer (as well as gradient ones)

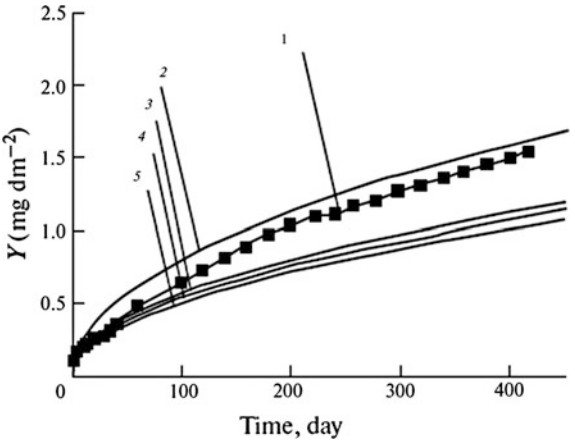

Fig. 5.9 Oxidation kinetics (T = 400 °C) of Zr with different GS: (*1*) experimental data for CG specimens; (*2*) estimated data for those specimens; (*3*, *4* and *5*) estimated values for GS of 29, 25 and 20 nm, respectively (adapted from [58])

coatings are presented in [62], where it was shown a perceptivity of compositionally graded coating structures for the operational service life growth. Other theoretical approaches of the corrosion studies towards multy-scale modeling of localized corrosion are presented in review [63], but such investigations are only starting and still practically have not connection with the NMs itself (as a rule, in such studies, the size effects are not taken in mind).

5.4 Examples of Applications

There are many data in literature concerning the nanostructured coating perspectives for the corrosion attack reduction in different systems. As an example, in Fig. 5.10, the kinetic curves are shown for the mass changes of the ASTM 1020 steel samples (in initial state and with various coatings) in a sulphate media at high temperatures [64]. The coatings-based Ni–Cr–C alloy were formed by the high-velocity air-fuel deposition method, using the standard CG powders and powders, being milled at low temperatures (in the latter case the GS was about 30–50 nm). The Fig. 5.10 data are clearly demonstrate that these coatings are considerably decreasing the corrosion actions at the sacrifice of a dense Cr_2O_3 film formation, being fixed by the XRD, SEM, and TEM methods, and as one would expect just the nanostructured coatings (curves 4 and 6) demonstrated the higher resistance and stability.

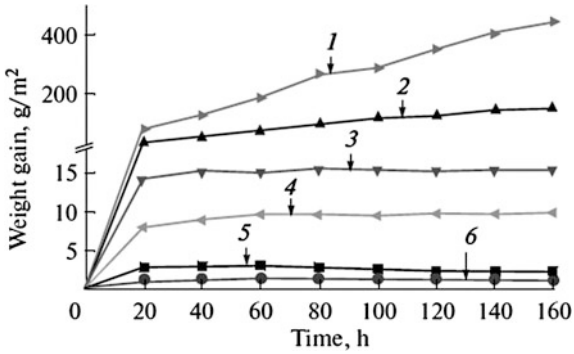

Fig. 5.10 Weight gain versus corrosion time for ASTM 1020 steel (curves *1* and *2*) and conventional coatings (those *3* and *5*) as well as nanostructured coatings (those *4* and *6*) in Na_2SO_4–30 % K_2SO_4 environment at 550 °C (curves *2*, *5* and *6*) and 650 °C (curves *1*, *3* and *4*) (adapted from [64])

In [64], it is marked out that the nanostructured coatings can be recommended for the boiler tubes protection. Other examples of some nanostructured coatings effective applications for the corrosion protection with specific aims are presented in the following publications: the Ni-based superalloy nanocrystalline protective coating in NaCl acidic solution [65]; nanostructured NiCoCrAlY coatings for oxidation protection [66]; Ni-based superalloy K36 (with Y addition) for molten sulfate at 900 °C [67]; HfC/SiC multi-layer coatings for the protection of carbon composites [68]; nanostructured CoNiCrAlYSi coatings for cyclic hot corrosion in molten salt at 880 °C up to 640 h [69]. In [65–67, 69], it was marked an accelerated formation of the passivation films-based Cr_2O_3 and Al_2O_3.

For comparison purposes in Table 5.8, the data, concerning some nitride nanoparticles (NbN, VN, CrN, and TiN) and their behavior in the various liquid media, are summarized and systematized (the error of the v value definitions is about ±1 Å/day) [70].

It is worth noting that for the VN particles interaction with HNO_3 a total dissolution is observed, but at the same time, the TiN particles reaction form oxide. The most aggressive liquid medium turns to be alkaline solution. Under the studied conditions, the highest corrosion resistance has been revealed for the chromium oxide samples, and the authors [70] are even recommending this compound for a potential usage in the proton exchange membranes of the fuel elements.

The last achievements in the field of the nanostructured titanium alloys (as well as the multi-component bioactive nanocoatings on their basis), especially for the medical applications, are well known and were described and analyzed in details in many recent publications (e.g., [71–74]). Many of these materials have already demonstrated very perspective combination of the chemical, physical, tribological, and biologic properties, and therefore, many of these coatings are used or recommended for the various medical items fabrication (such as the implants, fixers, and artificial limbs; see also early Fig. 4.19). It was found also that some calcium-phosphates coatings, deposited on the implant surfaces, are raising their corrosion resistance in the physiological solutions and aggressive media [72, 74]. The recent data have also shown that the Ti-based metallic nanoglasses (of $Ti_{34}Zr_{14}Cu_{22}Pd_{30}$ type) offer a high compatibility with the biological media [75].

Accumulation of information about the corrosion properties of nanomaterials is very intensive and some of the most interesting recent issues are listed below:

1. Stress corrosion cracking of UFG and conventional Al–7.5Mg alloy [76];
2. Oxidation of ZrB_2 composites-based various transition metal silicides (such as $ZrSi_2$, $MoSi_2$, $TaSi_2$, and WSi_2) at T = 1200–1800 °C [77];
3. The effect of bulk and surface SPD on corrosion behavior corrosion fatigue of AA5083 aluminium alloy [78];
4. Comparative corrosion behavior of Zr–20 % Cr and Zr–20 % Ti alloy nanocrystalline films [79];
5. Factors controlling corrosion behavior of amorphous and nanocrystalline alloys [80].

Table 5.8 Change of the nanoparticles diameter (d), estimated by XRD, and corrosion rates (v) after treatment at 80 °C during 2 weeks in H_2O and 2M NaOH, HCl, HNO_3, and H_2SO_4 solutions (adapted from [70])

Nit-ride	d_o (nm)	H_2O		NaOH		HCl		HNO_3		H_2SO_4	
		d (nm)	v (Å/day)	d (nm)	v (Å/day)	d (nm)	v (Å/day)	d (nm)	v (Å/day)	d (nm)	v (Å/day)
NbN	23	22	0.3	20	1.0	22	0.3	17	2.1	21	0.7
VN	35	27	2.8	20	5.3	35	0	diss	–	20	5.3
CrN	31	32	(−0.3)	29	0.7	31	0	30	0.3	29	0.7
TiN	28	23	1.7	22	2.1	26	0.7	oxide	–	22	2.1

References

1. Koch CC, Ovid'ko IA, Seal S et al (2007) Structural Nanocrystalline Materials: Fundamentals and Applications. Cambridge University Press, Cambridge
2. Saji VS, Thomas J (2007) Nanomaterials for corrosion control. Curr Sci 92:51–55
3. Raiston KD, Birbilis N (2010) Effect of grain size on corrosion: a review. Corrosion 66:0750005 (1–13)
4. Liu L, LI Y, Wang F (2010) Electrochemical corrosion behavior of nanocrystalline materials—a review. J Mater Sci Technol 26:1–14
5. Maurice V, Marcus Ph (2012) Passive films at the nanoscale. Electrochim Acta 84:129–138
6. Andrievski RA (2013) The role of nanoscale effects in the interaction between nanostructured materials and environments. Prot Metals Phys Chem Surf 49:528–540
7. Mahesh BV, Singh Raman RK (2014) Role of nanostructure in electrochemical corrosion and high temperature oxidation: a review. Metall Mater Trans A 45:5799–5822
8. Erb U (2010) Size effects in electroformed nanomaterials. Key Eng Mater 444:163–188
9. Gupta RK, Singh Raman RK, Koch CC (2010) Fabrication and oxidation resistance of nanocrystalline Fe10Cr alloy. J Mater Sci 45:4884–4888
10. Rashidi AM (2011) Isothermal oxidation kinetics of nanocrystalline and coarse grained nickel: experimental results and theoretical approaches. Surf Coat Technol 205:4117–4123
11. Gupta RK, Birbilis N, Zhang J (2012) Oxidation resistance of nanocrystalline alloys. In: Shih H (ed) Corrosion Resistance. InTech, Croatia, pp 213–238 (Chapter 10)
12. Manesh BV, Singh Raman RK, Koch CC (2012) Bimodal grain sixe distribution: an effective approach for improving the mechanical properties of Fe–Cr–Ni alloy. J Mater Sci 47:7735–7743
13. Rotagha R, Langer R, El-Sherik AM et al (1991) The corrosion behavior of nanocrystalline nickel. Scr Metall Mater 25:2867–2872
14. Mishra R, Balasubramaniam R (2004) Effect of nanocrystalline grain size on the electrochemical and corrosion behavior of nickel. Corr Sci 46:3019–3029
15. Kim SH, Aust KT, Erb U et al (2003) A comparison of the corrosion behavior of polycrystalline and nanocrystalline cobalt. Scr Mater 48:1379–1384
16. Luo W, Shi P, Wang Ch et al (2012) Electrochemical corrosion behavior of bulk nanocrystalline copper in nitric acid solution. J Electrochem Soc 159:C80–C85
17. Erb U (2011) Corrosion behavior of electrodeposited nanocrystal. In: Winston R (ed) Uhlig's corrosion handbook, 3rd edn. John Wiley & Sons, West Sussex, pp 517–528 (Chapter 37)
18. Zhao Y, Cheng IC, Kassner ME et al (2014) The effect of nanotwins on the corrosion behavior of copper. Acta Mater 67:181–188
19. Syugaev AV, Lomeva SF, Reshetnikov SM (2010) Electrochemical properties of nanocrystalline α-Fe + Fe_3C composites in acid mediums. Prot Metals Phys Chem Surf 46(1):82–88
20. Afshari V, Dehghanian C (2010) The effect of pure iron in a nanocrystalline grain size on the corrosion inhibitor behavior of sodium benzoate in near-neutral aqueous solution. Mater Chem Phys 124:466–471
21. Umoren SA, Li Y, Wang FH (2011) Influence of iron microstructure on the performance of polyacrylic acid as corrosion inhibitor in sulfuric acid solution. Corr Sci 53:1778–1785
22. Wang SG, Sun M, Cheng PC et al (2011) The electrochemical corrosion of bulk nanocrystalline ingot iron in HCl solution with different concentration. Mater Chem Phys 127:459–464
23. Gupta RK, Singh Raman RK, Koch CC (2012) Electrochemical characteristics of nano-and microcrystalline Fe–Cr alloys. J Mater Sci 47:6118–6124
24. Hoseini M, Shahryari A, Omanovic S et al (2009) Comparative effect of grain size and texture on the corrosion behavior of commercially pure titanium processed by equal channel angular pressing (2009) Corr Sci 51:3064–3067

25. Nie M, Wang ChT, Qu M et al (2014) The corrosion behavior of commercial purity titanium processed by high-pressure torsion. J Mater Sci 49:2824–2831
26. Amirhanova NA, Valiev RZ, Chernyaeva EYu et al (2010) Corrosion behavior of titanium materials with an ultrafine-grained structure. Russ Metall (Metally) 2010(5):456–460
27. Chuvil'deev VN, Kopylov VI, Bakhmet'ev et al (2012) Effect of the simultaneous enhancement in strength and corrosion resistance of microcrystalline titanium alloys. Doklady Phys 57:10–13
28. Bozhko PV, Korshunov AV, Il'in AP et al (2012) Reactive capacity of submicrocrystalline titanium. II. Electrochemical properties and corrosion resistance in sulphuric acid solutions. Perspective Mater 5:13–20 (in Russian)
29. Korshunov AV, Il'in AP, Lotkov AI et al (2012) Reactive capacity of submicrocrystalline titanium. I. Regularities of oxidation during air heating. Perspective Mater 4:5–12 (in Russian)
30. Mathur Sh, Jain R, Kumar P et al (2012) Effect of nanocrystalline phase on the electrochemical behavior of the alloy $Ti_{60}Ni_{40}$. J All Comp 538:160–163
31. Nikulin SA, Rogachev SO, Rozhnov AB et al (2012) Resistance of alloy Zr–2.5 % Nb with ultrafine-grain structure to stress corrosion cracking. Met Sci Heat Treatm 54:407–418
32. Argade GR, Kumar N, Mishra RS (2013) Stress corrosion cracking susceptibility of ultrafine grained Al–Mg–Sc alloy. Mater Sci Eng, A 565:80–89
33. Brunner JG, Birbilis N, Ralston KD et al (2012) Impact of ultrafine-grained microstructure on the corrosion of aluminium alloy AA2024. Corr Sci 57:209–214
34. Vrátná J, Hadzima B, Bukovina M et al (2013) Room temperature corrosion properties of AZ31 magnesium alloy processed by extrusion and equal channel angular pressing. J Mater Sci 48:4510–4516
35. Youssef KhMS, Koch CC, Fedkiw PS (2004) Improved corrosion behavior of nanocrystalline zinc produced by pulse-current electrodeposition. Corr Sci 46:51–64
36. Li MCh, Jiang LL, Zhang WQ et al (2007) Electrochemical corrosion behavior of nanocrystalline zinc coatings in 3.5 % NaCl solutions. J Sol State Electroch 11:1319–1325
37. Voitovich VB, Lavrenko VA, Adejev VM (1994) High-temperature oxidation of titanium boride of different purity. Oxid Met 42:145–161
38. Andrievski RA, Lavrenko VA, Desmaison J et al (2000) High-temperature oxidation of AlN-base films. Doklady Phys Chem 373:99–101
39. Lavrenko VA, Panasyuk AD, Desmaison-Brut M et al (2005) Kinetics and mechanism of electrochemical corrosion of titanium-based ceramics in 3 % NaCl solution. J Eur Cer Soc 25:1813–1818
40. Dranenko AC, Lavrenko VA, Talash VN (2010) Corrosion stability of nanostructured TiB_2 films in 3 % NaCl solution. Powder Metall Met Cer 49(3–4):74–178
41. Dranenko AC, Lavrenko VA, Talash VN (2013) Corrosion resistance of TiN films in 3 % NaCl solution. Powder Metall Met Cer 52(3–4): 223–227
42. Pan X, Shen K, Xu J et al (2012) Preparation and corrosion resistance of TiB_2 amorhous-crystalline films. Chin J Electr Dev 35:135–138
43. Barkovskaya MM, Uglov VV, Khodasevich VV (2011) Composition and corrosion resistance of coatings on the basis of nitrides of titanium and chromium. J Surf Invest 5:402–409
44. Her Sh-Ch, Wu Ch-L (2012) Corrosion resistance of TiN coating on 304 steel. Appl Mech Mater 121–126:3779–3783
45. Kuptsov KA, Kiryukhantsev-Korneev PhV, Sheveiko AN et al (2013) Comparative study of electrochemical and impact wear behavior of TiCN, TiSiCN, TiCrSiCN, and TiAlSiCN coatings. Surf Coat Techn 216:273–281
46. Bondarev AV, Kiryukhantsev-Korneev PhV, Sheveiko AN et al (2015) Structure, tribological and electrochemical properties of low friction TiAlSiCN/MoSeC coatings. Appl Surf Sci 327:253–261
47. Conde A, Navas C, Cristobal AB et al (2006) Characterization of corrosion and wear behaviour of nanoscaled e-beam PVD CrN coatings. Surf Coat Techn 201:2690–2695
48. Larijani MM, Elmi M, Yari M et al (2009) Nitrogen effect on corrosion resistance of ion beam sputtered nanocrystalline zirconium nitride films. Surf Coat Techn 203:2591–2594

49. Escobar C, Villareall M, Caicedo JC et al (2013) Diagnostic of corrosion-erosion evolution for [Hf-Nitrides/V-Nitrides]*n* structures. Thin Sol Films 545:194–199
50. Escobar C, Caicedo JC, Aperator W et al (2014) Corrosion resistant surface for vanadium nitride and hafnium nitride layers as a function of grain size. J Phys Chem Sol 75:23–30
51. Grigoriev ON, Galanov BA, Lavrenko VA et al (2010) Oxidation of ZrB_2–SiC–$ZrSi_2$ ceramics in oxygen. J Eur Cer Soc 30:2397–2405
52. Fahrenholtz WG, Hilmas GE (2012) Oxidation of ultra-high temperature transition metal diboride ceramics. Int Mater Rev 57:61–72
53. Carney C, Paul A, Venugopal S et al (2014) Qualitative analysis of hafnium diboride based ultra high temperature ceramics under oxyacetylene torch testing at temperatures above 2100 °C. J Eur Cer Soc 34:1045–1051
54. Gherrab M, Garnier V, Gavarini S et al (2013) Oxidation behavior of nano-scaled and micro-scaled TiC powders. Int J Refr Met Hard Mater 41:590–596
55. Kurlov AS, Gusev AI (2013) Oxidation of tungsten carbide powders in air. Int J Refr Met Hard Mater 41:300–307
56. Zhao G, Zhang X, Shen Zh et al (2014) Oxidation of ZrB_2 nanoparticles at high temperature under low oxygen pressure. J Am Ceram Soc 97:2360–2363
57. Musil J (2012) Hard nanocomposites coatings: thermal stability, oxidation resistance and toughness. Surf Coat Techn 207:50–65
58. Zhang XY, Shi MH, Li C et al (2007) The influence of grain size on the corrosion resistance of nanocrystalline zirconium metal. Mater Sci Eng, A 448:259–263
59. Ralston KD, Birbilis N, Davies CHJ (2010) Revealing the relationship between grain size and corrosion rate of metals. Scr Mater 63:1201–1204
60. Volonakis G, Tsetseris L, Logothetidis S (2011) Electronic and structural properties of TiB_2: bulk, surface, and nanoscale effects. Mater Sci Eng B 176:484–489
61. Bouzoubaa A, Diawara B, Maurice V et al (2009) Ab initio modeling of localized corrosion: study of the role of surface steps in the interaction of chlorides with passivated nickel surfaces. Corr Sci 51:2174–2182
62. Cross SR, Woolham R, Shademan S et al (2013) Computational design and optimization of multilayered and functionally graded corrosion coatings. Corr Sci 77:297–307
63. Gunasegaram DR, Venkatraman MS, Cole IS (2014) Towards multiscale modeling of localized corrosion. Int Mater Rev 59:84–114
64. Tao K, Zhou X, Cui H et al (2008) Preparation and properties of a nanostructured NiCrC alloy coating for boiler tubes protection. Mater Trans 49:2159–2162
65. Liu L, Li Y, Wang F (2008) Influence of grain size on the corrosion behavior of a Ni-based superalloy nanocrystalline coating in NaCl acidic solution. Electrochim Acta 53:2453–2462
66. Mercier D, Gauntt BD, Brochu M (2011) Thermal stability and oxidation behavior of nanostructured NiCoCrAlY coatings. Surf Coat Technol 205:4162–4168
67. Yu P, Wang W, Wang F et al (2011) High-temperature corrosion behavior of sputtered K38 nanocrystalline coatings with and without yttrium addition in molten sulfate at 900 °C. Surf Coat Technol 206:68–74
68. Verdon C, Szwedek O, Jacques S et al (2013) Hafnium and silicon carbide multilayer coatings for the protection of carbon composites. Surf Coat Technol 230:124–129
69. Yaghtin AH, Javadpour S, Shariat MH (2014) Hot corrosion of nanostructured CoNiCrAlYSi coatings deposited by high velocity oxy fuel process. J All Comp 584:303–307
70. Yang M, Allen AJ, Nguyen MT et al (2013) Corrosion behavior of mesoporous transition metal nitrides. J Sol St Chem 205:49–56
71. Kolobov YuR (2010) Nanotechnologies for the formation of medical implants based on titanium alloys with bioactive coatings. Nanotechnol Russ 4:758–775
72. Shtansky DV, Levashov EA (2013) Recent progress in the field of multicomponent bioactive nanostructured films. RCS Adv 3:11107–11115
73. Mishnaevsky L Jr, Levashov E, Valiev RZ et al (2014) Nanostructured titanium-based materials for medical implants: modeling and development. Mater Sci Eng R 81:1–19

74. Lyakhov NZ (ed) (2014) Biocomposites on base of calcium-phosphate coatings, nanostructural and ultra-fined grained bioinert metals, their biocompatibility and biodegrdation. Publ House Tomsk St Univ, Tomsk (in Russian)
75. Gleiter H, Schimmel Th, Han H (2014) Nanostructured solids – from nano-glasses to quantum transistors. Nano Today 9:17–66
76. Sharma MM, Tomedi JD, Weigley TJ (2014) Slow strain rate testing and stress corrosion cracking of ultra-fine grained and conventional Al–Mg. Mater Sci Eng A 619:35–45
77. Silverstroni L, Meriggi G, Sciti D (2014) Oxidation behavior of ZrB_2 composites doped with various transition metal silicides. Corr Sci 83:281–291
78. Abdulstaar M, Mhaede M, Wollmann M et al (2014) Investigating the effect of bulk and surface severe plastic deformation on the fatigue, corrosion behavior and corrosion fatigue of AA5083. Surf Coat Technol 254:244–251
79. Ali F, Mehmood M, Gasim AM et al (2014) Comparative study of the structure and corrosion behavior of Zr–20 %Cr and Zr–20 %Ti alloy films deposited by multi-arc ion plating technique. Thin Sol Films 564:277–281
80. Królikowski A (2015) Corrosion behavior of amorphous and nanocrystalline alloys. Solid State Phenom 227:11–14